The Astrophysical Journal Letters, 943:L16 (14pp), 2023 February 1 https://doi.org/10.3847/2041-8213/acb0cd

Redder than Red: Discovery of an Exceptionally Red L/T Transition Dwarf

Adam C. Schneider[1], Adam J. Burgasser[2], Justice Bruursema[1], Jeffrey A. Munn[1], Frederick J. Vrba[1], Dan Caselden[3], Martin Kabatnik[4], Austin Rothermich[3], Arttu Sainio[4], Thomas P. Bickle[4,5], Scott E. Dahm[1], Aaron M. Meisner[6], J. Davy Kirkpatrick[7], Genaro Suárez[3], Jonathan Gagné[8,9], Jacqueline K. Faherty[3], Johanna M. Vos[3], Marc J. Kuchner[10], Stephen J. Williams[1], Daniella Bardalez Gagliuffi[11], Christian Aganze[2], Chih-Chun Hsu[2], Christopher Theissen[2], Michael C. Cushing[12], Federico Marocco[7], and Sarah Casewell[13]
The Backyard Worlds: Planet 9 Collaboration

[1] United States Naval Observatory, Flagstaff Station, 10391 West Naval Observatory Road, Flagstaff, AZ 86005, USA; aschneid10@gmail.com
[2] Center for Astrophysics and Space Science, University of California San Diego, La Jolla, CA 92093, USA
[3] Department of Astrophysics, American Museum of Natural History, Central Park West at 79th Street, New York, NY 10024, USA
[4] Backyard Worlds: Planet 9, USA
[5] School of Physical Sciences, The Open University, Milton Keynes, MK7 6AA, UK
[6] NSF's National Optical-Infrared Astronomy Research Laboratory, 950 N. Cherry Avenue, Tucson, AZ 85719, USA
[7] IPAC, Mail Code 100-22, Caltech, 1200 E. California Boulevard, Pasadena, CA 91125, USA
[8] Planétarium Rio Tinto Alcan, Espace pour la Vie, 4801 avenue Pierre-de Coubertin, Montréal, QC H1V 3V4, Canada
[9] Institute for Research on Exoplanets, Université de Montréal, 2900 Boulevard Édouard-Montpetit, Montréal, QC H3T 1J4, Canada
[10] Exoplanets and Stellar Astrophysics Laboratory, NASA Goddard Space Flight Center, 8800 Greenbelt Road, Greenbelt, MD 20771, USA
[11] Department of Physics & Astronomy, Amherst College, 25 East Drive, Amherst, MA 01003, USA
[12] Ritter Astrophysical Research Center, Department of Physics and Astronomy, University of Toledo, 2801 W. Bancroft St., Toledo, OH 43606, USA
[13] School of Physics and Astronomy, University of Leicester, University Road, Leicester, LE1 7RH, UK
Received 2022 December 16; revised 2022 December 30; accepted 2023 January 4; published 2023 January 31

Abstract

We present the discovery of CWISE J050626.96+073842.4 (CWISE J0506+0738), an L/T transition dwarf with extremely red near-infrared colors discovered through the Backyard Worlds: Planet 9 citizen science project. Photometry from UKIRT and CatWISE give a $(J-K)_{\rm MKO}$ color of 2.97 ± 0.03 mag and a $J_{\rm MKO} - {\rm W2}$ color of 4.93 ± 0.02 mag, making CWISE J0506+0738 the reddest known free-floating L/T dwarf in both colors. We confirm the extremely red nature of CWISE J0506+0738 using Keck/NIRES near-infrared spectroscopy and establish that it is a low-gravity, late-type L/T transition dwarf. The spectrum of CWISE J0506+0738 shows possible signatures of CH_4 absorption in its atmosphere, suggesting a colder effective temperature than other known, young, red L dwarfs. We assign a preliminary spectral type for this source of L8γ–T0γ. We tentatively find that CWISE J0506+0738 is variable at 3–5 μm based on multiepoch WISE photometry. Proper motions derived from follow-up UKIRT observations combined with a radial velocity from our Keck/NIRES spectrum and a photometric distance estimate indicate a strong membership probability in the β Pic moving group. A future parallax measurement will help to establish a more definitive moving group membership for this unusual object.

Unified Astronomy Thesaurus concepts: Brown dwarfs (185); L dwarfs (894); T dwarfs (1679)

Supporting material: data behind figure

1. Introduction

Young L dwarfs are often noted to be redder than their field-age counterparts (Kirkpatrick et al. 2008; Cruz et al. 2009; Faherty et al. 2013, 2016; Liu et al. 2016). This is partly due to their lower surface gravities, which lead to lower pressures in their atmospheres, and hence reduced collision-induced absorption by H_2 (Linsky 1969). Further, lower surface gravities can lead to higher-altitude clouds, leading to less efficient gravitational settling of condensate particles (e.g., Madhusudhan et al. 2011; Helling et al. 2014). Red near-infrared colors have been efficiently utilized to characterize and discover new young brown dwarfs and planetary-mass objects (e.g., Kellogg et al. 2015; Schneider et al. 2017). There also exists a population of red L dwarfs that do not have obvious signs of youth (e.g., Looper et al. 2008; Kirkpatrick et al. 2010; Marocco et al. 2014). While the exact reasons for the red colors of these relatively high-gravity objects are not entirely clear, their spectra have been well reproduced by the presence of micron- or submicron-sized grains in their upper atmospheres (Marocco et al. 2014; Hiranaka et al. 2016; Charnay et al. 2018). This high-altitude dust suppresses emission at shorter wavelengths much more efficiently than at longer wavelengths, leading to significantly reddened spectra compared to "normal" brown dwarfs. There is evidence that the strength of silicate absorption features in the mid-infrared correlates with the near-infrared colors of L dwarfs (Burgasser et al. 2008; Suárez & Metchev 2022), indicating that variations in silicate cloud thickness also play a role. Further, viewing angle (Vos et al. 2017) and variability (Ashraf et al. 2022) have been shown to be related to the colors of substellar objects. There is also evidence that convective instabilities can produce similar effects as clouds in young, red L dwarfs (Tremblin et al. 2017). In any case, young, red L dwarfs and old reddened L dwarfs have proven to be compelling laboratories for the study of low-temperature substellar atmospheres.

The vast majority of the current population of directly imaged planetary-mass companions are also young and have similar effective temperatures, masses, and radii to young L dwarfs, as well as observed properties, including unusually red near-infrared colors. Examples include 2M1207b (Chauvin et al. 2004, 2005; Patience et al. 2010), HD 206893B (Delorme et al. 2017; Milli et al. 2017; Kammerer et al. 2021; Meshkat et al. 2021; Ward-Duong et al. 2021), VHS J125601.92−125723.9B (Gauza et al. 2015), 2MASS J22362452+4751425b (Bowler et al. 2017), BD+60 1417B (Faherty et al. 2021), HR8799bcd (Marois et al. 2008), and HD 203030B (Metchev & Hillenbrand 2006). Young, red L dwarfs in the field provide an opportunity to study the physical properties of giant exoplanet-like atmospheres without the technical challenge of blocking host starlight.

In this article, we present the discovery of CWISE J050626.96+073842.4 (CWISE J0506+0738), an exceptionally red brown dwarf discovered as part of the Backyard Worlds: Planet 9 (BYW) citizen science project (Kuchner et al. 2017). We detail its discovery in Section 2, present Keck/NIRES spectroscopic follow-up observations in Section 3, analyze these data in Section 4, and discuss CWISE J0506+0738 in the context of other red brown dwarfs in Section 5.

2. Discovery of CWISE 0506+0738

CWISE J0506+0738 was submitted as an object of interest to the BYW project by citizen scientists Austin Rothermich, Arttu Sainio, Sam Goodman, Dan Caselden, and Martin Kabatnik because it had notable motion among epochs of WISE observations. BYW uses unWISE images (Lang 2014; Meisner et al. 2018) covering the 2010–2016 time frame and is typically sensitive to objects with proper motions $\gtrsim$0.″05–0.″1 yr^{-1}. As part of the initial investigation to evaluate whether or not CWISE J0506+0738 was a newly discovered substellar object, we gathered available photometry from the Two Micron All-Sky Survey (2MASS) reject catalog (Skrutskie et al. 2006; 2MASS Team 2006), the United Kingdom Infrared Telescope (UKIRT) Hemisphere Survey DR1 (UHS; Dye et al. 2018), and the CatWISE 2020 main catalog (Marocco et al. 2021) and determined a photometric spectral type of ∼L7.5 using the method described in Schneider et al. (2016a). It was noted during the initial evaluation of this object that its $J-K$ color, using UHS J- and 2MASS K-band photometry, was exceptionally red ($J-K=3.17\pm0.21$ mag), more than half a magnitude redder than the reddest known free-floating L dwarf, PSO J318.5338−22.8603 ($J-K=2.64\pm0.02$ mag; Liu et al. 2013a). An inspection of 2MASS, UHS, WISE, and Pan-STARRS DR2 (Magnier et al. 2020) images showed no sources of contamination, suggesting that the near-infrared colors accurately reflect the true spectral energy distribution of the source (Figure 1).

The astrometry and photometry of CWISE J0506+0738 were further analyzed using measurements from the UHS DR2 catalog, which will provide K-band photometry for much of the northern hemisphere (J. Bruursema et al. 2023, in preparation). CWISE J0506+0738 was found to have a K-band magnitude of 15.513 ± 0.022 mag, consistent with the previous 2MASS measurement but significantly more precise. This measurement results in a UHS $(J-K)_{\rm MKO}$ color of 3.24 ± 0.10 mag, slightly redder but consistent with UHS and 2MASS photometry. We therefore considered this candidate a high-priority target for follow-up spectroscopic observations.

3. Observations

3.1. UKIRT/WFCAM

In an effort to refine the astrometry and photometry of CWISE J0506+0738, we observed it with the $J_{\rm MKO}$ filter on the infrared Wide-Field Camera (WFCAM; Casali et al. 2007) on UKIRT on 2022 September 20. Observations were performed using a 3×3 microstepping pattern, with the resulting nine images interleaved (Dye et al. 2006) to provide improved sampling over that of a single WFCAM exposure. The microstepping sequence was repeated 5 times, resulting in 45 single exposures, each lasting 20 s, for a total exposure time of 900 s. We reregistered the world coordinate system of each interleaved frame using the Gaia DR3 catalog (Gaia Collaboration et al. 2022). Images were then combined using the `imstack` routine from the `CASUTOOLS` package[14] (Irwin et al. 2004). The position and photometry of CWISE J0506+0738 were extracted using the `CASUTOOLS imcore` routine.

Combining the position of this J-band observation with the UHS K-band observation, we calculated proper motion components of $\mu_\alpha=31.5\pm2.6$ mas yr^{-1} and $\mu_\delta=-82.7\pm2.7$ mas yr^{-1}. CatWISE 2020 reports proper motions of $\mu_\alpha=44.2\pm7.9$ mas yr^{-1} and $\mu_\delta=-97.5\pm8.4$ mas yr^{-1} (with offset corrections applied according to Marocco et al. 2021). The proper motion calculated from our UKIRT observations is significantly more precise than the proper motion measurements from CatWISE 2020, and we adopt the former for our analysis.

We measure a $J_{\rm MKO}-$band magnitude of 18.487 ± 0.017 mag from these observations, which is $>2\sigma$ brighter than the value from the UHS (18.76 ± 0.10 mag). To verify our measured photometry, we compared the photometry for other sources found to have similar magnitudes ($18.4<J<18.6$ mag) in our images to UHS values. We found a median J-band difference for the 52 objects in this sample to be −0.03 mag, with a median absolute deviation of 0.07 mag, showing that differences as large as those measured for this object (0.27 mag) are relatively rare. The origin of the difference between these J-band measurements is unclear though we note that variability may be a contributing factor as young (and red) objects are often found to have larger amplitude variability than field-age objects with similar spectral types (e.g., Vos et al. 2022a). While this new J-band measurement results in bluer $(J-K)_{\rm MKO}=2.97\pm0.03$ mag and $J_{\rm MKO}-{\rm W2}=4.94\pm0.02$ mag colors, they both remain significantly redder than those of any previously identified free-floating brown dwarf.

All UKIRT photometry and astrometry for CWISE J0506+0738 are provided in Table 1.

3.2. Keck/NIRES

CWISE J0506+0738 was observed with the Near-Infrared Echellette Spectrometer (NIRES; Wilson et al. 2004) mounted on the Keck II telescope on UT 2022 January 19. NIRES provides a resolution $\lambda/\Delta\lambda\approx2700$ over five cross-dispersed orders spanning a wavelength range of 0.9–2.45 μm. CWISE J0506+0738 was observed in four 250 s exposures nodded in an ABBA pattern along the slit, which was aligned with the parallactic angle, for a total on-source integration time of 1000 s. The spectrum was extracted using a modified version of the SpeXTool package (Vacca et al. 2003; Cushing et al. 2004), with the A0 V star HD 37887 ($V=7.67$) used for telluric correction. The large $J-K$

[14] http://casu.ast.cam.ac.uk/surveys-projects/software-release

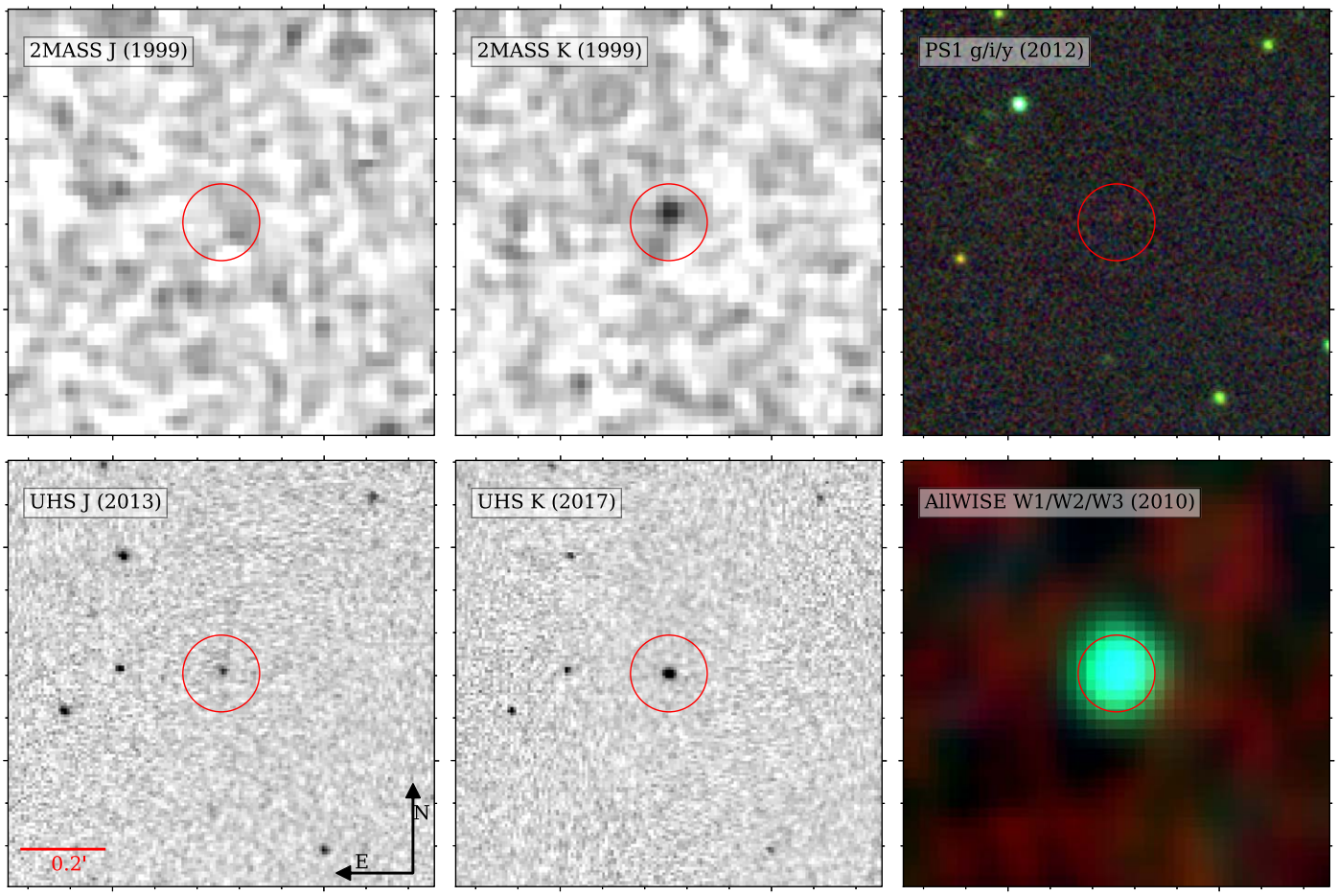

Figure 1. Images of CWISE J0506+0738 from 2MASS (upper left and center), UHS (bottom left and center), Pan-STARRS (upper right; three-color image with $g/i/y$ bands), and AllWISE (WISE Team 2020d) (lower right; three-color image with W1/W2/W3 bands). The position of CWISE J0506+0738 as determined in the UHS K-band images is denoted by a red circle. Note that CWISE J0506+0738 is undetected at 2MASS J and in the Pan-STARRS three-color image but clearly detected in the 2MASS K-band, UHS, and WISE images. The greenish hue of CWISE J0506+0738 in the WISE images shows that this object is significantly brighter at WISE channel W2 (4.6 μm) than at WISE channel W1 (3.4 μm) or W3 (12 μm), typical of brown dwarfs with late-L or later spectral types.

Table 1
Properties of CWISE J050626.96+073842.4

Parameter	Value	References
R.A. (°) (epoch = 2022.7)[a]	76.6124377	1
Decl. (°) (epoch = 2022.7)[a]	7.6449299	1
R.A. (°) (epoch = 2017.8)[a]	76.6123885	2
Decl. (°) (epoch = 2017.8)[a]	7.6450716	2
μ_α (mas yr^{-1})	31.5 ± 2.6	1
μ_δ (mas yr^{-1})	-82.7 ± 2.7	1
d[b] (pc)	32^{+4}_{-3}	1
RV (km s^{-1})	$+16.3^{+8.8}_{-7.7}$	1
$J_{\rm MKO}$ (mag)	18.487 ± 0.017	1
$K_{\rm MKO}$ (mag)	15.513 ± 0.022	2
W1 (mag)	14.320 ± 0.015	3
W2 (mag)	13.552 ± 0.013	3
Sp. Type	L8γ–T0γ	1

Notes.
[a] R.A. and decl. values are given in the International Celestial Reference System.
[b] Photometric distance estimate based on the UHS $K_{\rm MKO}$-band magnitude and the absolute magnitude-spectral type relation in Dupuy & Liu (2012) (see Section 5.3).
References. (1) This work; (2) UHS DR2 (Dye et al. 2018; J. Bruursema et al. 2023, in preparation); (3) CatWISE 2020 (Marocco et al. 2021).

color of CWISE J0506+0738 resulted in significant signal-to-noise ratio (S/N) differences across the final reduced spectrum, with an S/N $\sim$ 25 at the J-band peak ($\sim$1.3 μm) and an S/N $\sim$ 200 at the K-band peak ($\sim$2.2 μm).

The interband flux calibration for Keck/NIRES orders is occasionally skewed by seeing or differential refraction slit losses. In particular, there is a gap between the third (K-band) and fourth (H-band) orders spanning 1.86 to 1.89 μm,[15] and the overlap between the fourth and fifth (J-band) orders lies in a region of strong telluric and stellar H_2O absorption. We therefore rescaled the resulting spectrum to have a $J-K$ synthetic color consistent with UKIRT J-band and UHS K-band photometry by applying small multiplicative constants to the H- and K-band portions of the spectrum. The final reduced spectrum is shown in Figure 2.

4. Analysis

4.1. Spectral Type

As with many of the known, young, late-type red L dwarfs, none of the L dwarf spectral standards (Kirkpatrick et al. 2010; Cruz et al. 2018) provide a suitable match to the near-infrared

[15] https://www2.keck.hawaii.edu/inst/nires/genspecs.html

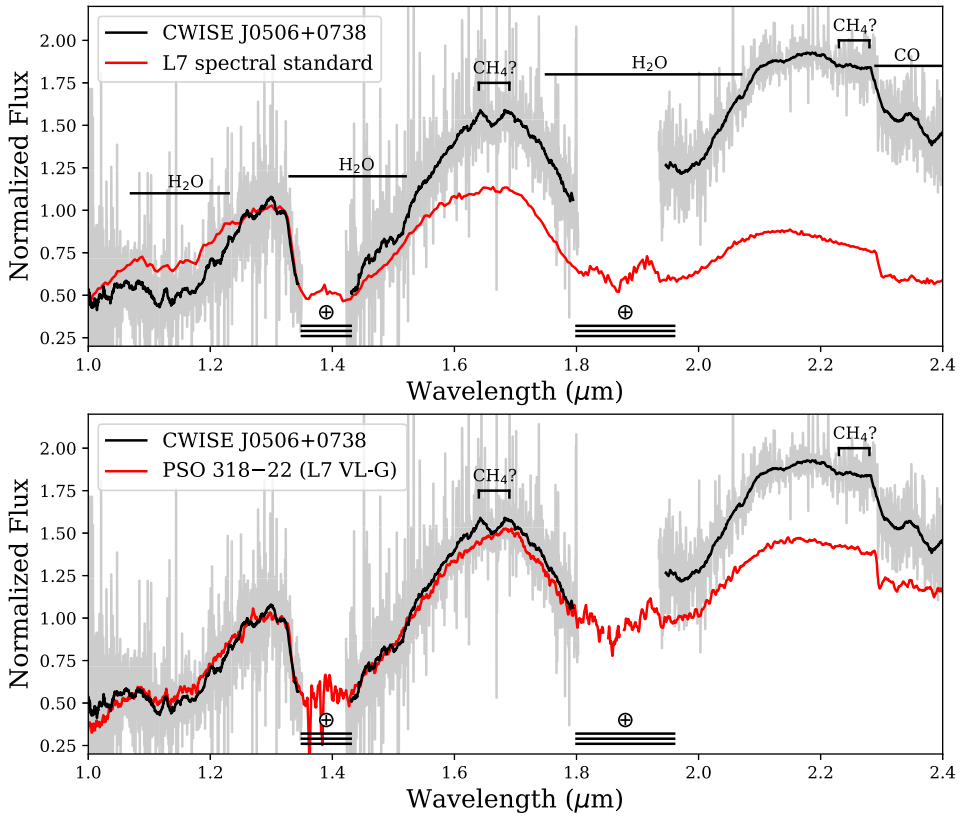

Figure 2. The Keck/NIRES spectrum of CWISE J0506+0738, shown in the original resolution (gray lines) and smoothed to a resolution of $\lambda/\Delta\lambda \approx 100$ (black lines). CWISE J0506+0738 is compared to the L7 spectral standard 2MASSI J0825196+211552 (Kirkpatrick et al. 2000; Cruz et al. 2018) in the upper panel and to the young L7 VL-G dwarf PSO J318.5338−22.8603 (Liu et al. 2013a) in the lower panel. Both comparisons highlight the extremely red nature of CWISE J0506+0738. All spectra are normalized between 1.27 and 1.29 μm, and prominent absorption features have been labeled.

(The data used to create this figure are available.)

spectrum of CWISE J0506+0738. The best match to the *J*-band portion of the spectrum is the L7 standard 2MASSI J0825196 +211552 (Kirkpatrick et al. 1999; Cruz et al. 2018), which is shown in the upper panel of Figure 2. CWISE J0506+0738 shows much stronger H_2O absorption around 1.1 μm, a feature commonly seen in low-gravity L dwarfs. This comparison also shows how red CWISE J0506+0738 is compared to a normal, field-age/field-gravity late L dwarf. The lower panel of Figure 2 shows a comparison of CWISE J0506+0738 with PSO J318.5338−22.8603 (Liu et al. 2013a), which is typed as L7 VL-G. These two objects match relatively well across the *J*-band portion of the spectrum though the extreme redness of CWISE J0506+0738 can still be seen in this comparison via the mismatch in the *H*- and *K*-band portions of their spectra.

We also note that the spectrum of CWISE J0506+0738 has a noticeable absorption feature at the *H*-band peak. There is also a second, less-pronounced absorption feature present in the *K*-band portion of CWISE J0506+0738's spectrum between 2.2 and 2.3 μm. While we cannot a priori rule out systematic noise or a data reduction artifact for these features, we note that no similar features have been seen in Keck/NIRES spectra of L dwarfs obtained and reduced by our group (e.g., Meisner et al. 2021; Schapera et al. 2022; Softich et al. 2022; Theissen et al. 2022). We also note that these features occur at the approximate locations of CH_4 absorption seen in model spectra of low-surface gravity brown dwarfs with effective temperatures $\lesssim$1400 K. Figure 3 compares solar-metallicity model spectra from Marley et al. (2021) with fixed low-surface gravities ($\log(g) = 3.5$) and varying effective temperatures. Prominent methane absorption features can be seen in the *H* and *K* bands for $T_{\rm eff} \lesssim 1400$ K. While these models are informative for (potentially) identifying the source of some of the absorption features seen in the spectrum of CWISE J0506 +0738, we were unable to find any models that successfully reproduced the overall shape of CWISE J0506+0738's spectrum, similar to previous studies of young brown dwarfs (e.g., Manjavacas et al. 2014).

The presence of CH_4 in the *H*- and *K*-band peaks of CWISE J0506+0738's spectrum would suggest that this source is early T dwarf (Burgasser et al. 2006) although these features are fairly weak in strength. Charnay et al. (2018) showed that the presence of clouds can greatly reduce the abundance of CH_4 in the photospheres of low-gravity objects, a possible explanation for the absence of CH_4 bands in the spectra of 2M1207b and HR8799bcd (Barman et al. 2011a, 2011b; Konopacky et al. 2013). If the same effect holds here, it would argue for a particularly low temperature for CWISE J0506+0738, below that of the $T_{\rm eff} \approx 1200$ K planetary-mass L dwarf PSO J318.5338 −22.8603 and VHS 1256−1257B, which originally showed no indication of CH_4 absorption in the 1–2.5 μm region.[16] (Liu et al. 2013a; Gauza et al. 2015). These two sources do have detectable absorption in the 3.3 μm ν_3 CH_4 fundamental band

[16] Recent high S/N JWST/NIRSPEC observations of VHS 1256−1257B have revealed the presence of weak 1.6 μm absorption in its spectrum (Miles et al. 2022).

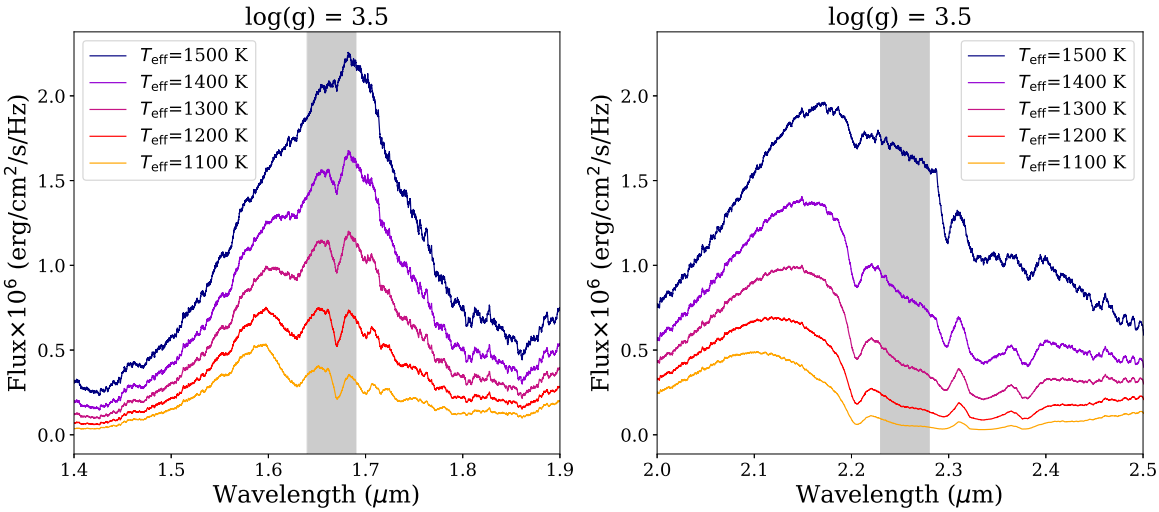

Figure 3. Model spectra from Marley et al. (2021) with varying effective temperatures and surface gravity fixed at $\log(g) = 3.5$. The gray bands highlight the approximate regions of the absorption features seen in the spectrum of CWISE J0506+0738.

(Miles et al. 2018), and cloud scattering opacity is likely responsible for muting the 1.6 and 2.2 μm bands in these red L dwarfs (Charnay et al. 2018; Burningham et al. 2021). Indeed, it has been noted previously that PSO J318.5338−22.8603 is just on the warmer side of the transition to CH_4 becoming the dominant carbon-bearing molecule in its atmosphere (Tremblin et al. 2017). We tentatively assert that both *H*- and *K*-band features in the spectrum of CWISE J0506+0738 are due to CH_4 absorption, which may be tested with more detailed analysis (e.g., atmospheric retrievals; Burningham et al. 2017, 2021) and higher S/N moderate-resolution data. Given the similarity of the *J*-band portion of CWISE J0506+0738's spectrum to PSO J318.5338−22.8603 (L7 VL-G) and the likely detection of CH_4 in the *H* and *K* bands, we assign a near-infrared spectral type of L8γ–T0γ to CWISE J0506+0738, where the γ signifies very low surface gravity (Kirkpatrick 2005).

4.2. Spectral Evidence of Youth

The characterization of brown dwarfs and planetary-mass objects as "low surface gravity" or "young" typically arises from gravity-sensitive (or more specifically, photosphere pressure-sensitive) spectral features quantified by spectral indices (e.g., Steele & Jameson 1995; Martin et al. 1996; Luhman et al. 1997; Gorlova et al. 2003; McGovern et al. 2004; Kirkpatrick et al. 2006; Allers et al. 2007; Manjavacas et al. 2020). Many of these spectral indices, however, are designed for optical spectra (e.g., Cruz et al. 2009) or are only applicable to objects with spectral types earlier than ∼L5 (e.g., Allers & Liu 2013; Lodieu et al. 2018). The *H*-cont index is a gravity-sensitive index defined in Allers & Liu (2013) that is one of the few gravity-sensitive indices applicable to spectral types later than L5. This index is designed to approximate the slope of the blue side of the *H*-band peak, with low-gravity objects exhibiting a much steeper slope than field-age brown dwarfs. However, this index is defined using a band centered at 1.67 μm, which is where a feature potentially attributable to CH_4 occurs in our spectrum. Thus the *H*-cont index does not provide an accurate assessment of the slope of the blue side of the *H*-band peak for this object.

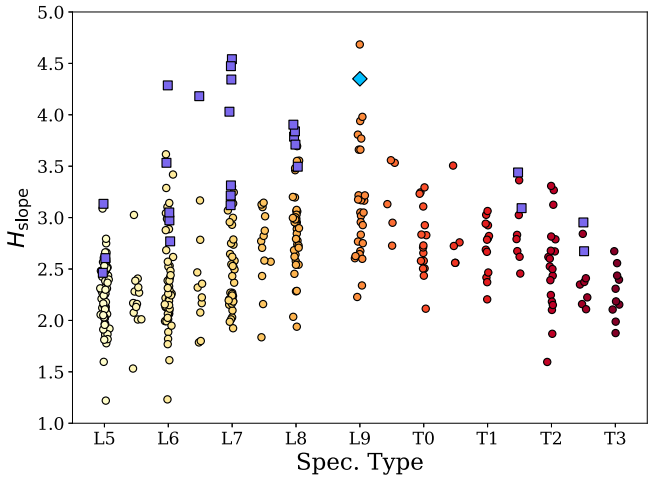

Figure 4. *H*-band slope index vs. spectral type for field late-L and T dwarfs (colored circles) based on data from the SPLAT archive (Burgasser 2017), with colors corresponding to spectral type. Young L and T dwarfs are represented by purple squares. CWISE J0506+0738 (blue diamond) is an outlier among field-age late-Ls, similar to the young, late-type L dwarf population. Small offsets have been added to spectral type values for differentiation purposes.

We have created a modified slope index for the blue side of the *H*-band peak by computing a simple linear least-squares fit to the 1.45–1.64 μm region after normalizing to the *J*-band peak between 1.27 and 1.29 μm. We measured this slope (normalized flux/μm) for several late-L and early-T dwarfs, both field and young association members, as shown in Figure 4. We note that the largest slope for the entire sample belongs to WISE J173859.27+614242.1, an object that has been difficult to classify (Mace et al. 2013), but is most consistent with an extremely red L9 (Thompson et al. 2013). It is unclear if this object is young, has an extremely dusty photosphere, or both. For typical L7-T0 dwarfs, *H*-slope values for field objects range from 2 to 4, while equivalently classified young L dwarfs have values that range over 3–5. For CWISE J0506+0738, we find a slope of 4.38, significantly larger than field-age late-L dwarfs. The known population of young, very red L dwarfs similarly has larger *H*-slope values than their field-age counterparts.

Schneider et al. (2014) also showed that the $H_2(K)$ index defined in Canty et al. (2013) could distinguish young, low-gravity late-L dwarfs from the field late-L population. The $H_2(K)$ index determines the slope of the K band between 2.17 and 2.24 μm. CWISE J0506+0738 has an $H_2(K)$ value of 1.030, which is again consistent with the known population of low-gravity late-type L dwarfs ($1.029 \leqslant H_2(K) \leqslant 1.045$) compared to field-age L6–L8 brown dwarfs ($H_2(K) \gtrsim 1.05$).

Another spectral feature that has been used to distinguish low-surface gravity late-L dwarfs are the K I absorption lines between 1.1 and 1.3 μm (McGovern et al. 2004; Allers & Liu 2013; Miles et al. 2022). Our Keck/NIRES spectrum does not have sufficient S/N around the J-band peak to investigate these lines. A higher S/N spectrum would help to ensure no ambiguity regarding the surface gravity of CWISE J0506+0738.

4.3. Radial Velocity

The resolution of the Keck/NIRES data is sufficient to obtain a coarse measure of the radial velocity (RV) of CWISE J0506+0738, particularly in the vicinity of strong molecular features. We followed a procedure similar to that described in (Burgasser et al. 2015; see also Blake et al. 2010; Hsu et al. 2021), forward-modeling the wavelength-calibrated spectrum prior to telluric correction in the 2.26–2.38 μm region. This spectral band contains the prominent 2.3 μm CO 2–0 band present in L dwarf spectra, as well as strong telluric features that allow refinement of the spectral wavelength calibration (see Newton et al. 2014). We used a $T_{\rm eff} = 1300$ K, $\log g = 4.5$ dex (cgs) BTSettl atmosphere model ($M[\lambda]$) from Allard et al. (2012), which provides the best match to the CO band strength, and a telluric absorption model ($T[\lambda]$) from Livingston (1991). We forward-modeled the data ($D[\lambda]$) using four parameters: the barycentric RV of the star ($RV_\oplus$), the strength of telluric absorption (α), the instrumental Gaussian broadening profile width ($\sigma_{\rm broad}$), and the wavelength offset from the nominal SpeXtool solution ($\Delta\lambda$):

$$D[\lambda] = (M[\lambda^* + \Delta\lambda] \times T[\lambda + \Delta\lambda]^\alpha) \otimes \kappa_G(\sigma_{\rm broad}), \quad (1)$$

with $\lambda^* = \lambda(1 + RV_\oplus/c)$ accounting for the radial motion of the star and κ_G representing the Gaussian broadening kernel. Preliminary fits that additionally included rotational broadening of the stellar spectrum indicated that this parameter was equal to the instrumental broadening and is likely unresolved $v \sin i \lesssim 65$ km s^{-1}), so it was ignored in our final fit.

After an initial "by-eye" optimization of parameters, we used a simple Markov Chain Monte Carlo (MCMC) algorithm to explore the parameter space, evaluating goodness of fit between model and data using a χ^2 statistic. Figure 5 displays the posterior distribution of our fit parameters after removing the first half of the MCMC chain ("burn-in"), which is normally distributed. There is a small correlation between $RV_\oplus$ and $\Delta\lambda$, which is expected given that stellar and telluric features are intermixed in this region. This correlation increases the uncertainties of these parameters. We find that the best-fit model from this analysis is an excellent match to the NIRES spectrum, with residuals consistent with uncertainties. After correction for barycentric motion (-19.2 km s^{-1}), we determine a heliocentric RV of $+16.3^{+8.8}_{-7.7}$ km s^{-1} for CWISE J0506+0738.

5. Discussion

5.1. Redder than Red

CWISE J0506+0738 has exceptionally red colors compared to the known brown dwarf population. Figure 6 highlights this by comparing CWISE J0506+0738 to other UHS DR2 L and T dwarfs (A. Schneider et al. 2023, in preparation) and red L dwarfs not covered by the UHS survey. Table 2 summarizes photometric and spectral type information for all known free-floating L dwarfs with $J - K$ colors greater than 2.2 mag. All photometry is on the Mauna Kea Observatories (MKO) system and comes from Liu et al. (2016), Best et al. (2021), or the VISTA Hemisphere Survey (VHS; McMahon et al. 2013). WISE J173859.27+614242.1 has no near-infrared MKO photometry in the literature or in available catalogs. For this source, we used its low-resolution near-infrared spectrum published in Mace et al. (2013) normalized to its most precise K-band photometric measurement (2MASS K_S; Skrutskie et al. 2006), and then computed synthetic $J_{\rm MKO}$ and $K_{\rm MKO}$ photometry. Even among known red L dwarfs, CWISE J0506+0738 stands out as exceptionally red, being ~0.3 mag redder in both $(J - K)_{\rm MKO}$ and $J_{\rm MKO} - W2$ color than all other known free-floating L dwarfs.

Directly imaged planetary-mass companions also have exceptionally red near-infrared colors. Some of the L-type companions (Table 2) do not have WISE W1 (3.4 μm) and W2 (4.6 μm) photometry but have equivalent Spitzer/IRAC photometry in ch1 (3.6 μm) and ch2 (4.5 μm). For HD 203030B, we use J- and K-band photometry from Metchev & Hillenbrand (2006) and Miles-Páez et al. (2017) and convert Spitzer/IRAC ch1 and ch2 photometry from Martinez & Kraus (2022) using the Spitzer-WISE relations from Kirkpatrick et al. (2021). For VHS 1256−1257B, we use J- and K-band photometry from Gauza et al. (2015) and convert Spitzer/IRAC ch2 photometry from Zhou et al. (2020) to W2 using the Kirkpatrick et al. (2021) relation. We chose not to use the published W1 photometry of VHS 1256−1257B from Gauza et al. (2015) because of its large uncertainty (0.5 mag). For BD +60 1417B, all photometry comes directly from Faherty et al. (2021). Both HD 203030B and BD+60 1417B are included in both panels of Figure 6, while VHS 1256−1257B is included in the left panel of Figure 6. We note that none of these companions have $(J - K)_{\rm MKO}$ or $J_{\rm MKO} - W2$ colors as red as CWISE J0506+0738. Of the remaining planetary-mass companions that lack 3–5 μm photometry, only 2M1207b ($J - K = 3.07 \pm 0.23$ mag; Chauvin et al. 2004, 2005; Mohanty et al. 2007; Patience et al. 2010) and HD 206893B ($J - K = 3.36 \pm 0.08$ mag; Delorme et al. 2017; Milli et al. 2017; Kammerer et al. 2021; Meshkat et al. 2021; Ward-Duong et al. 2021) have redder $J - K$ colors than CWISE J0506+0738.

5.2. WISE Photometric Variability

Young brown dwarfs have been shown to have enhanced photometric variability compared to field-age brown dwarfs (Biller et al. 2015; Metchev et al. 2015; Schneider et al. 2018; Vos et al. 2020, 2022a). Most brown dwarfs with detected variability at 3–5 μm, measured largely with Spitzer/IRAC, have amplitudes of a few percent or less (see compilation in Vos et al. 2020). Multiepoch photometry from WISE generally does not have the precision to detect such variability (Mace 2015; H. Brooks et al. 2023, in preparation). However,

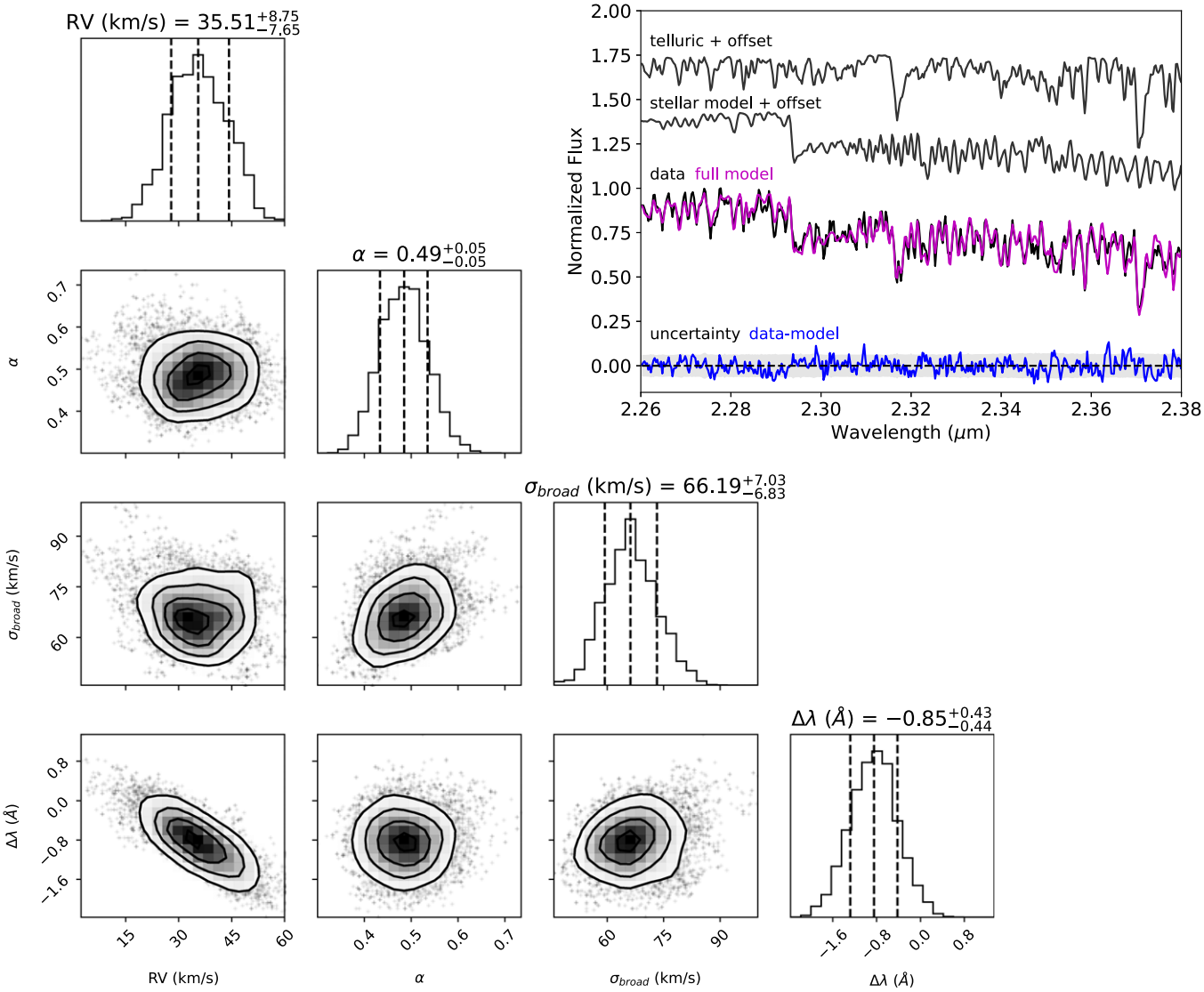

Figure 5. MCMC forward-model fit of the normalized 2.26–2.38 μm spectrum of CWISE J0506+0738 for RV measurement. The panels along the upper left to lower right diagonal show the posterior distributions for our four fitting parameters: the barycentric RV of the star ($RV_{\oplus}$ in km s^{-1}), the strength of the telluric absorption (α), the instrumental Gaussian broadening profile width (σ_{broad} in km s^{-1}), and the wavelength offset from the nominal SpeXtool solution ($\Delta\lambda$ in Å). The six lower left panels illustrate correlations between parameters; only the RV and $\Delta\lambda$ parameters show a modest inverse correlation, effectively expanding the uncertainty on the RV measurement. The upper right panel shows the NIRES spectrum of CWISE J0506+0738 prior to telluric correction (black line) and the best-fit model spectrum (magenta line) composed of stellar model and telluric absorption components (offset lines above fit). Residuals (data minus model; blue line) are consistent with measurement uncertainties (gray band).

objects with extremely high-amplitude variability could be distinguished in multiepoch WISE data.

Given tentative evidence of near-infrared photometric variability (see Section 3.1), we investigated WISE (Wright et al. 2010) and NEOWISE (Mainzer et al. 2011, 2014) data for evidence of mid-infrared variability for CWISE J0506+0738. WISE/NEOWISE have been scanning the mid-infrared sky for over 10 yr, and a typical location on the sky has been observed with the W1 and W2 filters every six months since early 2010.[17] During each ∼1 day visit, 10–15 individual exposures are typically acquired. We chose to analyze these single exposures as opposed to epochal coadds (e.g., "unTimely"; Meisner et al. 2022) because CWISE J0506+0738 is brighter than the nominal threshold where single-exposure photometry becomes unreliable, especially at W2 (∼14.5 mag; Schneider et al. 2016a), and the concern that the coadded frames would dilute any traces of photometric variability. Such coadded photometry may prove useful for future investigations of long-term/long-period variability.

We gathered photometry from the WISE/NEOWISE Single-exposure Source Catalogs (WISE Team 2020a, 2020b, 2020c; NEOWISE Team 2020) for CWISE J0506+0738 and the same set of known L, T, and Y dwarfs shown in Figure 6. Collectively, these objects should have comparable levels of low-amplitude variability generally undetectable by WISE. For each source, we measured the average and standard deviations of both W1 and W2 magnitudes. We omit frames with *qual_frame* values equal to zero as these frames likely have contaminated flux measurements. Because single-exposure frames are subject to astronomical transients (e.g., cosmic ray hits, satellite streaks), we excluded 4σ outliers from the set of

[17] With the exception of a ∼3 yr gap between the initial WISE mission and reactivation as NEOWISE from 2011 February to 2013 December.

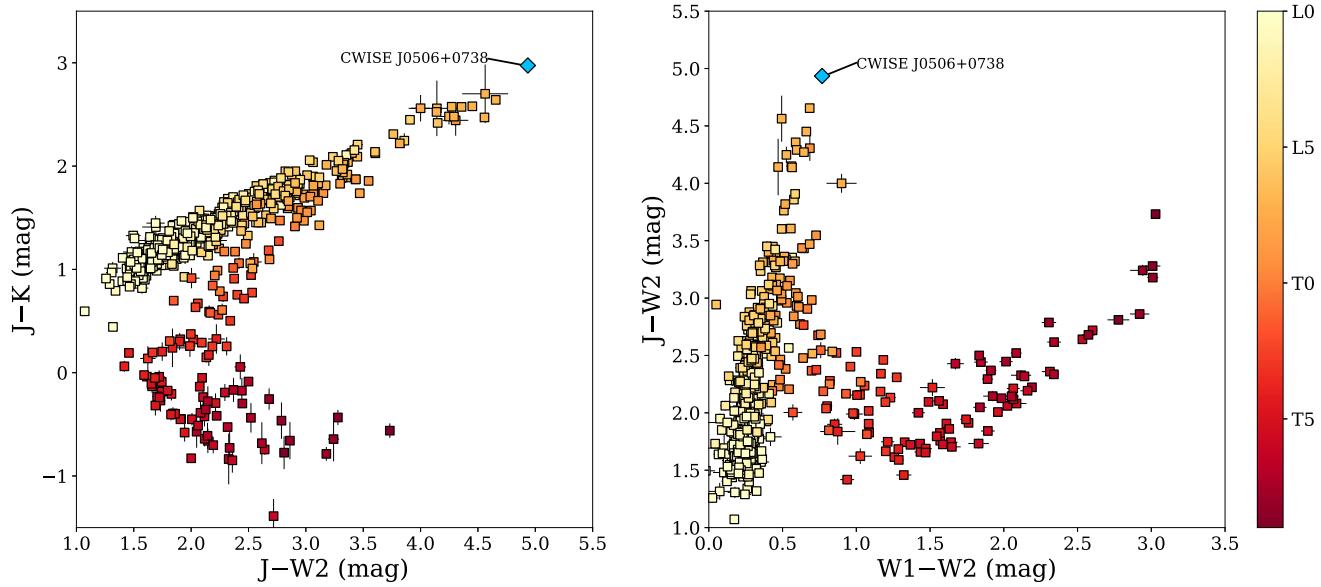

Figure 6. Color–color diagrams showing known brown dwarfs recovered in the UHS (A. Schneider et al. 2023, in preparation), supplemented with known red L dwarfs from Table 2. CWISE J0506+0738 is a clear outlier, being significantly redder than other known L dwarfs both in $J-K$ and $J-$ W2 colors.

single-exposure photometry for each source. We also excluded sources that were either blended or contaminated (e.g., bright star halos, diffraction spikes).

Figure 7 compares mean and standard deviation values, which show clear trends in both W1 and W2 photometry. We immediately identify four objects with magnitudes between 12 and 14.5 that have photometric scatter above the 5%–95% confidence interval ($\gtrsim 2\sigma$) in either W1 or W2.

2MASS 21392676+0220226 (2MASS J2139+0220) is a T1.5 dwarf (Burgasser et al. 2006) that is well-known for its large-amplitude infrared variability. Radigan et al. (2012) monitored 2MASS J2139+0220 and found J-band variability with a peak-to-peak amplitude of ∼26%, which until recent observations of VHS 1256−1257B (Zhou et al. 2022) was the highest amplitude variability found for any brown dwarf. Since the Radigan et al. (2012) study, this object has been the subject of numerous variability investigations (Apai et al. 2013; Khandrika et al. 2013; Karalidi et al. 2015), with Yang et al. (2016) finding variability of 11%–12% in Spitzer/IRAC ch1 and ch2 photometry. The extreme variability of 2MASS J2139 +0220 is attributed to variations in the thickness of silicate clouds (Apai et al. 2013; Karalidi et al. 2015; Vos et al. 2022b). This object has also been shown to have a nearly edge-on inclination (Vos et al. 2017) and is a kinematic member of the ∼200 Myr old Carina-Near moving group (Zhang et al. 2021).

WISE J052857.68+090104.4 (WISE J0528+0901) is a clear W1 outlier, originally classified as a late-M giant by Thompson et al. (2013) but later reclassified as a very low-gravity L1 brown dwarf member of the ∼20 Myr 32 Orionis group (Burgasser et al. 2016). This planetary-mass object has an anomalous $J-$ W2 color, suggestive of excess flux at 5 μm, although Burgasser et al. (2016) found no evidence of circumstellar material or cool companions. The source may also be variable in the W2 band, but its fainter magnitude here makes it less distinct than comparably bright L and T dwarfs. Nevertheless, these data suggest that WISE J0528+0901 has an unusually dusty and variable atmosphere, making it a compelling source for future photometric monitoring.

PSO J318.5338−22.8603 is a clear W2 outlier and an exceptionally red β Pic member that has been shown to have large-amplitude infrared variability in the infrared (Biller et al. 2015; Vos et al. 2019), with a peak-to-peak amplitude of 3.4% in Spitzer/IRAC ch2 photometry (Biller et al. 2018). Interestingly, PSO J318.5338−22.8603 is an outlier in W2 and not in W1, which may indicate cloud depth effects given that the W1 and W2 bands probe different depths in the atmosphere.

2MASSW J0310599+164816 (2MASS J0310+1648AB) is another W2 outlier and is an optically classified L8 (Kirkpatrick et al. 2000). This object is a resolved (0.″2) ∼equal brightness binary (Stumpf et al. 2010) that shows evidence of high-amplitude variability in the near-infrared (Buenzli et al. 2014). While the variability observations were not long enough to determine a true amplitude or period, the brightening rate of ∼2% per hour was the largest measured in the sample. While there is no clear evidence of youth for 2MASS J0310+1648AB in the literature, this object was typed as L9.5 (sl. red) in Schneider et al. (2014). Further investigation of the potential youth and cloud properties of this object may be warranted.

CWISE J0506+0738 joins this group of variability outliers as one of very few objects with both W1 and W2 scatter outside the 16%–84% confidence interval of comparable-brightness L and T dwarfs. To estimate the amplitude of variability associated with these deviations, we fit tenth-order polynomials to the scatter versus magnitude trends in W1 and W2 and calculated rms values by finding the magnitude offset (in quadrature) for our outlying targets. Assuming sinusoidal variability, rms values can be converted to peak-to-peak amplitudes with a multiplicative factor of $2\sqrt{2}$. Using the 16%–84% confidence region as uncertainties for the predicted values from the polynomial fits, we find peak-to-peak variability on the order of $13\% \pm 1\%$ for W1 and $12\% \pm 2\%$ for W2 for 2MASS J2139+0220, which is generally consistent with results from Spitzer (Yang et al. 2016). For CWISE J0506 +0738, we estimate $15\% \pm 5\%$ variability for W1 and $23\% \pm 9\%$ variability for W2. Variability at these levels would

Table 2
Infrared Photometry for L Dwarfs with $J - K > 2.2$ mag

Name	Discovery. References	SpT	SpT References	J_{MKO} (mag)	K_{MKO} (mag)	NIR References	W1 (mag)	W2 (mag)	$(J-K)_{MKO}$ (mag)	J_{MKO} − W2 (mag)
Free Floating										
WISEP J004701.06+680352.1	1	L6–L8γ	2	15.490 ± 0.070	13.010 ± 0.030	3	11.768 ± 0.010	11.242 ± 0.008	2.480 ± 0.076	4.248 ± 0.070
PSO 057.2893+15.2433	4	L7 red	4	17.393 ± 0.027	14.869 ± 0.012	20	13.818 ± 0.014	13.254 ± 0.012	2.524 ± 0.030	4.139 ± 0.030
2MASS J03552337+1133437	5	L3–L6γ	2	13.940 ± 0.003	11.491 ± 0.001	20	10.617 ± 0.012	10.032 ± 0.008	2.449 ± 0.003	3.908 ± 0.009
CWISE J050626.96+073842.4	6	L8–T0γ	6	18.487 ± 0.017	15.513 ± 0.022	6, 20	14.320 ± 0.015	13.552 ± 0.013	2.974 ± 0.028	4.935 ± 0.021
WISEA J090258.99+670833.1	7	L7 red	7	16.864 ± 0.246	14.305 ± 0.108	8	13.192 ± 0.013	12.722 ± 0.009	2.559 ± 0.269	4.142 ± 0.246
2MASS J11193254−1137466	9	L7 VL-G[a]	10	17.330 ± 0.029	14.751 ± 0.012	21	13.540 ± 0.014	12.879 ± 0.010	2.580 ± 0.032	4.451 ± 0.031
WISEA J114724.10−204021.3	11	L7γ	12	17.445 ± 0.028	14.872 ± 0.011	21	13.677 ± 0.013	13.088 ± 0.011	2.573 ± 0.030	4.357 ± 0.030
2MASS J16154255+4953211	13	L3–L6γ	2	16.506 ± 0.016	14.260 ± 0.070	3, 20	13.225 ± 0.012	12.648 ± 0.008	2.246 ± 0.072	3.858 ± 0.018
WISE J173859.27+614242.1	14	L9 pec(red)	14	17.680 ± 0.110[c]	15.237 ± 0.100[c]	6, 22	14.059 ± 0.011	13.374 ± 0.009	2.443 ± 0.149[c]	4.306 ± 0.100[c]
WISE J174102.78−464225.5	15	L5–L7γ	2	15.951 ± 0.010	13.533 ± 0.005	21	12.362 ± 0.027	11.802 ± 0.024	2.418 ± 0.011	4.149 ± 0.026
PSO J318.5338−22.8603	16	L7 VL-G	16	17.181 ± 0.018	14.540 ± 0.009	21	13.210 ± 0.013	12.526 ± 0.010	2.640 ± 0.020	4.655 ± 0.021
2MASS J21481628+4003593	17	L6.5 pec	17	14.054 ± 0.003	11.745 ± 0.001	20	10.801 ± 0.011	10.292 ± 0.007	2.309 ± 0.003	3.762 ± 0.008
ULAS J222711−004547	18	L7 pec	18	17.954 ± 0.039	15.475 ± 0.014	21[b]	14.259 ± 0.014	13.663 ± 0.013	2.479 ± 0.041	4.291 ± 0.041
2MASS J22443167+2043433	19	L6–L8γ	2	16.401 ± 0.016	13.826 ± 0.006	20	12.775 ± 0.012	12.130 ± 0.008	2.575 ± 0.017	4.271 ± 0.018
Companions										
BD+60 1417B	23	L6–L8γ	23	18.53 ± 0.20	15.83 ± 0.20	23	14.461 ± 0.014	13.967 ± 0.013	2.70 ± 0.28	4.46 ± 0.20
HD 203030B	24	L7.5	24	18.77 ± 0.08	16.21 ± 0.10	24, 25	15.67 ± 0.02[d]	14.77 ± 0.02[d]	2.56 ± 0.13	4.00 ± 0.08
VHS 1256−1257B	26	L7.5	26	17.136 ± 0.020	14.665 ± 0.010	21	⋯	12.579 ± 0.020[e]	2.471 ± 0.022	4.557 ± 0.028
2MASS J1207334−393254b	27, 28	L3 VL-G	29	20.0 ± 0.2	16.93 ± 0.11	27, 30	⋯	⋯	3.07 ± 0.23	⋯
HD 206893B	31	L4–L8	32	18.38 ± 0.03	15.02 ± 0.07	32	⋯	⋯	3.36 ± 0.08	⋯
2MASS J22362452+4751425b	33	late-L pec	33	19.97 ± 0.11	17.28 ± 0.04	33	⋯	⋯	2.69 ± 0.12	⋯
HR 8799b	34	L5–T2	35	19.46 ± 0.17	16.99 ± 0.06	36, 37, 38	⋯	⋯	2.47 ± 0.18	⋯

Notes.
[a] 2MASS J11193254−1137466 is a binary (Best et al. 2017), and the spectral type listed is the unresolved spectral type.
[b] ULAS J222711−004547 also has *J*- and *K*-band photometry in the UKIRT Large Area Survey (LAS; Lawrence et al. 2007). We use the VHS photometric measurements here because they have smaller uncertainties than those in the UKIRT LAS.
[c] Near-infrared photometry for WISE J173859.27+614242.1 was determined synthetically from its near-infrared spectrum.
[d] Converted from Spitzer ch1 and ch2 photometry in Miles-Páez et al. (2017) using relations in Kirkpatrick et al. (2021).
[e] Converted from Spitzer ch2 photometry in Zhou et al. (2020) using relations in Kirkpatrick et al. (2021).

References. (1) Gizis et al. (2012); (2) Gagné et al. (2015a); (3) Liu et al. (2016); (4) Best et al. (2015); (5) Reid et al. (2006); (6) This work; (7) Schneider et al. (2017); (8) Best et al. (2021); (9) Kellogg et al. (2015); (10) Best et al. (2017); (11) Schneider et al. (2016b); (12) Faherty et al. (2016); (13) Metchev et al. (2008); (14) Mace et al. (2013); (15) Schneider et al. (2014); (16) Liu et al. (2013b); (17) Looper et al. (2008); (18) Marocco et al. (2014); (19) Dahn et al. (2002); (20) UHS (Dye et al. 2018, J. Bruursema et al. 2023, in preparation); (21) VHS (McMahon et al. 2013); (22) 2MASS (Skrutskie et al. 2006); (23) Faherty et al. (2021); (24) Metchev & Hillenbrand (2006); (25) Miles-Páez et al. (2017); (26) Gauza et al. (2015); (27) Chauvin et al. (2004); (28) Chauvin et al. (2005); (29) Allers & Liu (2013); (30) Mohanty et al. (2007); (31) Milli et al. (2017); (32) Ward-Duong et al. (2021); (33) Bowler et al. (2017); (34) Marois et al. (2008); (35) Bowler et al. (2010); (36) Esposito et al. (2013); (37) Oppenheimer et al. (2013); (38) Liu et al. (2016).

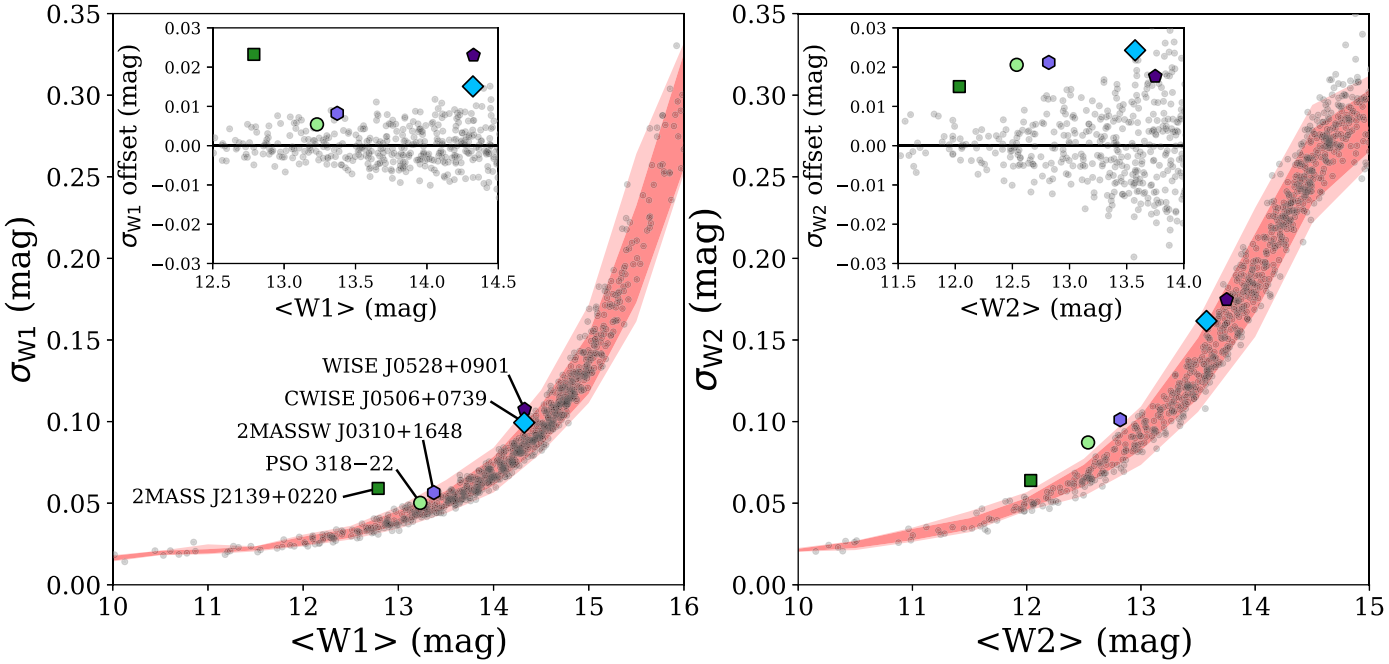

Figure 7. Standard deviation (σ) vs. average magnitude over all single-exposure WISE/NEOWISE W1 (left panel) and W2 (right panel) detections of known brown dwarfs. Color contours indicate 16%–84% and 5%–95% confidence intervals in 0.5 mag bins. The insets in each panel show the difference between measured σ values and polynomial fits to the magnitude trend. 2MASS J2139+0220 (dark green square), PSO J318.5338−22.8603 (light green circle), 2MASSW J0310599+164816 (light purple hexagon), CWISE J0506+0738 (cyan diamond), and WISE J052857.68+090104.4 (dark purple pentagon) are all highlighted as clear deviants from these trends.

certainly be extraordinary; however, we caution that the relatively low precision of WISE/NEOWISE single-exposure measurements may inflate these results. Future photometric and/or spectroscopic monitoring would help to explore the variability properties of CWISE J0506+0738.

5.3. Distance

CWISE J0506+0738 is faint at optical wavelengths and was therefore undetected by the Gaia mission (Gaia Collaboration et al. 2022). The currently available astrometry for CWISE J0506+0738 is insufficient for a parallax measurement. Because CWISE J0506+0738 has such an unusually shaped spectrum, standard spectral type versus absolute magnitude relations for normal, field-age brown dwarfs are not applicable. There have been efforts to create relations between absolute magnitudes and spectral types for low-gravity brown dwarfs; however, these are typically valid for spectral types earlier than L7 (e.g., Faherty et al. 2016; Liu et al. 2016). Faherty et al. (2013) found absolute photometry of the young L5 dwarf 2MASS J03552337+1133437 was fainter than field L5 dwarfs at wavelengths shorter than $\sim$2.5 μm, and brighter at longer wavelengths. Schneider et al. (2016b) investigated other young, red L dwarfs with measured parallaxes and found that *K*-band photometry produced photometric distances that aligned well with parallactic distances. This trend was also noted in Filippazzo et al. (2015), Faherty et al. (2016), and Liu et al. (2016).

Here, we use nine young, free-floating brown dwarfs (Table 2) with measured parallaxes (Liu et al. 2016; Best et al. 2020; Kirkpatrick et al. 2021; Gaia Collaboration et al. 2022) to compare measured distances to photometric distances based on absolute magnitude-spectral type relations for $J_{\rm MKO}$, $K_{\rm MKO}$, W1, and W2 (Dupuy & Liu 2012; Kirkpatrick et al. 2021; Figure 8). Consistent with prior results, we find that

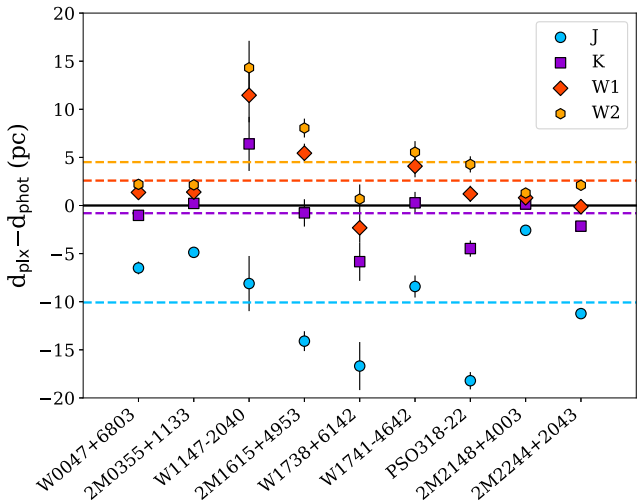

Figure 8. A comparison of photometric and parallactic distances for free-floating objects from Table 2 with measured parallaxes. Objects are labeled on the *x*-axis. Dashed lines show average differences between photometric and parallactic distances for each band, with colors corresponding to those given in the legend.

$K_{\rm MKO}$-band photometric distances (average offset $\Delta{\rm d} = -0.8$ pc, scatter $\sigma_d = 3.3$ pc) are generally more accurate than $J_{\rm MKO}$ ($\Delta{\rm d} = -10$ pc, $\sigma_d = 5.1$ pc), W1 ($\Delta{\rm d} = +2.6$ pc, $\sigma_d = 3.8$ pc), or W2 ($\Delta{\rm d} = +4.5$ pc, $\sigma_d = 4.1$ pc) photometric distances. To ensure these values are not biased, we also evaluated the fractional difference for each photometric band, defined as $\Delta{\rm d}/{\rm d}_{\rm plx}$, and find that *K*-band photometric distances are typically within 5% for this sample, compared to 52%, 11%, and 20% for $J_{\rm MKO}$, W1, and W2, respectively.

Using the absolute magnitude-spectral type relation from Dupuy & Liu (2012), a spectral type of L9 $\pm$ 1, and its

measured K_{MKO} photometry, we estimate a photometric distance of 32^{+4}_{-3} pc for CWISE J0506+0738. Again, given the exceptional nature of this source and its unknown multiplicity, we advise that this distance estimate be used with caution until it can be confirmed with a trigonometric parallax.

5.4. Moving Group Membership

Young brown dwarfs are often associated both spatially and kinematically with young, nearby moving groups, thereby serving as invaluable age benchmarks.

To assess the potential moving group membership of CWISE J0506+0738, we use the BANYAN Σ algorithm (Gagné et al. 2018a), which deploys a Bayesian classifier to assign probabilities of moving group membership through 6D coordinate alignment (position and velocity) to 26 known moving groups in the solar neighborhood. We used the position and proper motion of CWISE J0506+0738 from UKIRT and UHS measurements (Table 1) and our measured RV from the NIRES spectrum (Section 4.3). With these values alone, we find an 82% membership probability in the β Pictoris moving group (BPMG; Zuckerman et al. 2001), a 3% membership probability in the AB Doradus moving group (ABDMG; Zuckerman et al. 2004), and a 15% probability of being unassociated with any moving group. The predicted/optimal distances for membership in BPMG and ABDMG are 32 pc and 64 pc, respectively; our estimated distance clearly aligns with the former. If we include the distance estimate in the BANYAN Σ algorithm, the probability of BPMG membership goes up to 99%.

We also tested the kinematic membership of CWISE J0506+0738 using the LACEwING analysis code (Riedel et al. 2017). Again, using just the position, proper motion, and RV of CWISE J0506+0738, we find nonzero probabilities for ABDMG (56%), the Argus Moving Group (71%), BPMG (28%), the Columba Association (52%), and the Tucana-Horologium Association (6%). Note that LACEwING is stricter in assigning membership probabilities than BANYAN, with bona fide BPMG members having a maximum membership probability of ∼70% when only proper motion and RV are used (Riedel et al. 2017). If we use our photometric distance as an additional constraint, BPMG is returned as the group with the highest probability of membership at 86%.

Membership in the BPMG is clearly favored for CWISE J0506+0738 although a directly measured distance is necessary for confirmation. If confirmed, CWISE J0506+0738 would have the latest spectral type and lowest mass among free-floating BPMG members, following PSO J318.5338−22.8603 (Liu et al. 2013a). Several candidate members with L7 or later spectral types have also been proposed (Best et al. 2015; Schneider et al. 2017; Kirkpatrick et al. 2021; Zhang et al. 2021; however, see Hsu et al. 2021). PSO J318.5338−22.8603 has proven to be an exceptionally valuable laboratory for studying planetary-mass object atmospheres (Biller et al. 2015; Allers et al. 2016; Faherty et al. 2016; Biller et al. 2018). A second planetary-mass object in this group that bridges the L/T transition will further contribute to these studies.

Assuming β Pic membership, we can use the group age of 22 ± 6 Myr (Shkolnik et al. 2017) to estimate the mass of CWISE J0506+0738. To do this, we must first estimate the luminosity (L_{bol}) or effective temperature (T_{eff}) of the source. For the former, we used the empirical K-band bolometric correction/spectral type relation for young brown dwarfs quantified in Filippazzo et al. (2015). Combining this with the UHS K-band magnitude and our distance estimate, we infer a bolometric luminosity of $\log(L_{bol}/L_{\odot}) = -4.55 \pm 0.12$. We caution that this value is based on our estimated distance from Section 5.3 and will need to be updated when a measured parallax becomes available. We then used the solar-metallicity evolutionary models of Marley et al. (2021) to infer a mass of 7 ± 2 M_{Jup}. The evolutionary models also provide a radius of 1.32 ± 0.03 R_{Jup} for these parameters, consistent with the radii of low-gravity late-type L dwarfs (Filippazzo et al. 2015). Combining this radius with our bolometric luminosity, we find $T_{eff} = 1140 \pm 80$ K. This is ∼130 K cooler than a field-age L9 (Kirkpatrick et al. 2021), consistent with previous works showing low-gravity late-Ls tend to be ∼100–200 K cooler than field-age objects at the same spectral type (Filippazzo et al. 2015; Faherty et al. 2016). In particular, this temperature is 50–100 K cooler than T_{eff} estimates of PSO J318.5338−22.8603 (Liu et al. 2013a; Miles et al. 2018), consistent with the appearance of CH_4 absorption at lower temperatures.

The predicted mass of 7 ± 2 M_{Jup} is well below the deuterium-fusion minimum mass of 14 M_{Jup} commonly used to distinguish brown dwarfs from planetary-mass objects. As such, this object helps bridge the mass gap between the lowest mass free-floating β Pic members and directly imaged exoplanets, such as 51 Eri b (∼T6.5; Macintosh et al. 2015; Rajan et al. 2017). CWISE J0506+0738 could also help to constrain the effective temperature of the L/T transition at an age of ∼20–25 Myr (Binks & Jeffries 2014; Bell et al. 2015; Messina et al. 2016; Nielsen et al. 2016; Shkolnik et al. 2017; Miret-Roig et al. 2020). CWISE J0506+0738 would be one of the youngest objects to join a small but growing number of benchmark substellar objects with known ages at the L/T transition such as HD 203030B (30–150 Myr; Metchev & Hillenbrand 2006; Miles-Páez et al. 2017), 2MASS J13243553+6358281 (∼150 Myr; Looper et al. 2007; Gagné et al. 2018b), HIP 21152B, and other T-type Hyades members (∼650 Myr; Kuzuhara et al. 2022; Schneider et al. 2022), ϵ Indi Ba (∼3.5 Gyr; Scholz et al. 2003; Chen et al. 2022), and the white dwarf companion COCONUTS-1 (∼7 Gyr; Zhang et al. 2020).

6. Summary

We have presented the discovery and analysis of an exceptionally red brown dwarf, CWISE J0506+0738, identified as part of the BYW citizen science project. The near-infrared spectrum of CWISE J0506+0738 is highly reddened and shows signatures of low surface gravity, as well as weak absorption features that we associate with methane bands. This object has the reddest $J-K$ and $J-$W2 colors of any free-floating L-type brown dwarf, and we tentatively assign a near-infrared spectral type of L8γ–T0γ. The exceptionally red color of CWISE J0506+0738 may be due to several factors. Objects with low surface gravities have inefficient gravitational settling of silicate dust grains, which can remain high in the atmospheres. Such grains can be directly detected at long wavelengths (e.g., Cushing et al. 2006; Burgasser et al. 2008; Suárez & Metchev 2022) and could be constrained for CWISE J0506+0738 with future long-wavelength observations (e.g., Miles et al. 2022). The angle at which a brown dwarf is viewed has also been shown to affect its near-infrared colors, with objects viewed equator-on tending to have redder colors than

those viewed pole-on (Vos et al. 2017). A measurement of CWISE J0506+0738's rotational period combined with its rotational velocity (e.g., $v\sin i$) from a high-resolution spectrum could determine whether or not CWISE J0506+0738 is viewed closer to pole-on or equator-on. A high-resolution spectrum would also allow for a higher-precision RV measurement and a more detailed probe of gravity-sensitive features.

CWISE J0506+0738's astrometry and kinematics point to likely membership in the 22 Myr BPMG, to be confirmed or rejected with future trigonometric parallax and higher-precision RV measurements. If associated, CWISE J0506+0738 would be the lowest-mass β Pictoris member found to date, with an estimated mass of 7 ± 2 $M_{\rm Jup}$, well within the planetary-mass regime. The extreme colors of this object, and its relatively low proper motion ($<$100 mas yr^{-1}), suggest the existence of other extremely red L dwarfs that may have been missed by previous searches due to assumptions about brown dwarf colors or selection requirements for large proper motions. Recent large-scale near-infrared surveys such as UHS (Dye et al. 2018) and VHS (McMahon et al. 2013) that push several magnitudes deeper than previous efforts (e.g., 2MASS) may be able to confidently detect the faint J-band magnitudes of similar objects.

Because of this object's unique spectroscopic properties and the fact that young brown dwarfs often display large-amplitude variability (e.g., Vos et al. 2022a), CWISE J0506+0738 is an intriguing target for future photometric or spectroscopic variability monitoring. Longer-wavelength observations with the James Webb Space Telescope would have the additional advantage of further constraining the existence and abundance of CH_4 and analyzing the presence and properties of dust grains through silicate absorption features (Miles et al. 2022).

The Backyard Worlds: Planet 9 team would like to thank the many Zooniverse volunteers who have participated in this project. We would also like to thank the Zooniverse web development team for their work creating and maintaining the Zooniverse platform and the Project Builder tools. This research was supported by NASA grant 2017-ADAP17-0067. This material is supported by the National Science Foundation under grant No. 2007068, 2009136, and 2009177. This publication makes use of data products from the UKIRT Hemisphere Survey, which is a joint project of the United States Naval Observatory, The University of Hawaii Institute for Astronomy, the Cambridge University Cambridge Astronomy Survey Unit, and the University of Edinburgh Wide-Field Astronomy Unit (WFAU). UHS is primarily funded by the United States Navy. The WFAU gratefully acknowledges support for this work from the Science and Technology Facilities Council through ST/T002956/1 and previous grants. The authors acknowledge the support provided by the US Naval Observatory in the areas of celestial and reference frame research, including the USNO's postdoctoral program. (Some of) the data presented herein were obtained at the W. M. Keck Observatory, which is operated as a scientific partnership among the California Institute of Technology, the University of California and the National Aeronautics and Space Administration. The Observatory was made possible by the generous financial support of the W. M. Keck Foundation. This publication makes use of data products from the Wide-field Infrared Survey Explorer, which is a joint project of the University of California, Los Angeles, and the Jet Propulsion Laboratory/California Institute of Technology, and NEOWISE which is a project of the Jet Propulsion Laboratory/California Institute of Technology. WISE and NEOWISE are funded by the National Aeronautics and Space Administration. Part of this research was carried out at the Jet Propulsion Laboratory, California Institute of Technology, under a contract with the National Aeronautics and Space Administration. This publication makes use of data products from the Two Micron All Sky Survey, which is a joint project of the University of Massachusetts and the Infrared Processing and Analysis Center/California Institute of Technology, funded by the National Aeronautics and Space Administration and the National Science Foundation. This research has benefitted from the SpeX Prism Spectral Libraries, maintained by Adam Burgasser. The authors wish to recognize and acknowledge the very significant cultural role and reverence that the summit of Maunakea has always had within the indigenous Hawaiian community. We are most fortunate to have the opportunity to conduct observations from this mountain.

Facilities: UKIRT/WFCAM, Keck/NIRES, WISE, NEOWISE.

Software: BANYAN Σ (Gagné et al. 2018a), CASUTOOLS (Irwin et al. 2004), LACEwING (Riedel et al. 2017), SpeXTool (Cushing et al. 2004), SPLAT (Burgasser 2014), WiseView (Caselden et al. 2018).

ORCID iDs

Adam C. Schneider https://orcid.org/0000-0002-6294-5937
Adam J. Burgasser https://orcid.org/0000-0002-6523-9536
Justice Bruursema https://orcid.org/0000-0002-3858-1205
Jeffrey A. Munn https://orcid.org/0000-0002-4603-4834
Dan Caselden https://orcid.org/0000-0001-7896-5791
Martin Kabatnik https://orcid.org/0000-0003-4905-1370
Austin Rothermich https://orcid.org/0000-0003-4083-9962
Arttu Sainio https://orcid.org/0000-0003-4864-5484
Thomas P. Bickle https://orcid.org/0000-0003-2235-761X
Scott E. Dahm https://orcid.org/0000-0002-2968-2418
Aaron M. Meisner https://orcid.org/0000-0002-1125-7384
J. Davy Kirkpatrick https://orcid.org/0000-0003-4269-260X
Genaro Suárez https://orcid.org/0000-0002-2011-4924
Jonathan Gagné https://orcid.org/0000-0002-2592-9612
Jacqueline K. Faherty https://orcid.org/0000-0001-6251-0573
Johanna M. Vos https://orcid.org/0000-0003-0489-1528
Marc J. Kuchner https://orcid.org/0000-0002-2387-5489
Daniella Bardalez Gagliuffi https://orcid.org/0000-0001-8170-7072
Christian Aganze https://orcid.org/0000-0003-2094-9128
Chih-Chun Hsu https://orcid.org/0000-0002-5370-7494
Christopher Theissen https://orcid.org/0000-0002-9807-5435
Michael C. Cushing https://orcid.org/0000-0001-7780-3352
Federico Marocco https://orcid.org/0000-0001-7519-1700
Sarah Casewell https://orcid.org/0000-0003-2478-0120

References

2MASS Team 2006, 2MASS Survey Point Source Reject Table, IPAC, doi:10.26131/IRSA98
Allard, F., Homeier, D., & Freytag, B. 2012, RSPTA, 370, 2765
Allers, K. N., Jaffe, D. T., Luhman, K. L., et al. 2007, ApJ, 657, 511
Allers, K. N., & Liu, M. C. 2013, ApJ, 772, 79

Allers, K. N., Gallimore, J. F., Liu, M. C., et al. 2016, ApJ, 819, 133
Apai, D., Radigan, J., Buenzli, E., et al. 2013, ApJ, 768, 121
Ashraf, A., Bardalez Gagliuffi, D. C., Manjavacas, E., et al. 2022, ApJ, 934, 178
Barman, T. S., Macintosh, B., Konopacky, Q. M., et al. 2011a, ApJ, 733, 65
Barman, T. S., Macintosh, B., Konopacky, Q. M., et al. 2011b, ApJL, 735, L39
Bell, Cameron P. M., Mamajek, Eric E., & Naylor, Tim 2015, MNRAS, 454, 593
Best, W. M. J., Liu, M. C., Magnier, E. A., et al. 2015, ApJ, 814, 118
Best, W. M. J., Liu, M. C., Dupuy, T. J., et al. 2017, ApJL, 843, L4
Best, W. M. J., Liu, M. C., Magnier, E. A., et al. 2020, AJ, 159, 257
Best, W. M. J., Liu, M. C., Magnier, E. A., et al. 2021, AJ, 161, 42
Biller, B. A., Vos, J., Bonavita, M., et al. 2015, ApJL, 813, L23
Biller, B. A., Vos, J., Buenzli, E., et al. 2018, AJ, 155, 95
Binks, A. S., & Jeffries, R. D. 2014, MNRAS, 438, L11
Blake, C. H., Charbonneau, D., & White, R. J. 2010, ApJ, 723, 684
Bowler, B. P., Liu, M. C., Dupuy, T. J., et al. 2010, ApJ, 723, 850
Bowler, B. P., Liu, M. C., Mawet, D., et al. 2017, AJ, 153, 18
Buenzli, E., Apai, D., Radigan, J., et al. 2014, ApJ, 782, 77
Burgasser, A. J., Geballe, T. R., Leggett, S. K., et al. 2006, ApJ, 637, 1067
Burgasser, A. J., Looper, D. L., Kirkpatrick, J. D., et al. 2008, ApJ, 674, 451
Burgasser, A. J. 2014, in ASI Conf. Ser. 11, Int. Workshop on Stellar Spectral Libraries, ed. H. P. Singh (Hyderabad: Astronomical Society of India)
Burgasser, A. J., Gillon, M., Melis, C., et al. 2015, AJ, 149, 104
Burgasser, A. J., Lopez, M. A., Mamajek, E. E., et al. 2016, ApJ, 820, 32
Burgasser, A. J. & Splat Development Team 2017, in ASI Conf. Ser. 14, Int. Workshop on Spectral Stellar Libraries (Hyderabad: Astronomical Society of India), 7
Burningham, Ben, Marley, M. S., Line, M. R., et al. 2017, MNRAS, 470, 1177
Burningham, Ben, Faherty, Jacqueline K, Gonzales, Eileen C, et al. 2021, MNRAS, 506, 1944
Canty, J. I., Lucas, P. W., Roche, P. F., & Pinfield, D. J. 2013, MNRAS, 435, 2650
Casali, M., Adamson, A., Alves de Oliveira, C., et al. 2007, A&A, 467, 777
Caselden, D., Westin, P., Meisner, A., et al. 2018, WiseView: Visualizing motion and variability of faint WISE sources, Astrophysics Source Code Library, ascl:1806.004
Charnay, B., Bézard, B., Baudino, J.-L., et al. 2018, ApJ, 854, 172
Chauvin, G., Lagrange, A.-M., Dumas, C., et al. 2004, A&A, 425, L29
Chauvin, G., Lagrange, A.-M., Dumas, C., et al. 2005, A&A, 438, L25
Chen, M., Li, Y., Brandt, T. D., et al. 2022, AJ, 163, 288
Cruz, K. L., Kirkpatrick, J. D., & Burgasser, A. J. 2009, AJ, 137, 3345
Cruz, K. L., Núñez, A., Burgasser, A. J., et al. 2018, AJ, 155, 34
Cushing, M. C., Vacca, W. D., & Rayner, J. T. 2004, PASP, 116, 362
Cushing, M. C., Roellig, T. L., Marley, M. S., et al. 2006, ApJ, 648, 614
Dahn, C. C., Harris, H. C., Vrba, F. J., et al. 2002, AJ, 124, 1170
Delorme, P., Schmidt, T., Bonnefoy, M., et al. 2017, A&A, 608, A79
Dupuy, T. J., & Liu, M. C. 2012, ApJS, 201, 19
Dye, S., Warren, S. J., Hambly, N. C., et al. 2006, MNRAS, 372, 1227
Dye, S., Lawrence, A., Read, M. A., et al. 2018, MNRAS, 473, 5113
Esposito, S., Mesa, D., Skemer, A., et al. 2013, A&A, 549, A52
Faherty, J. K., Rice, E. L., Cruz, K. L., et al. 2013, AJ, 145, 2
Faherty, J. K., Riedel, A. R., Cruz, K. L., et al. 2016, ApJS, 225, 10
Faherty, J. K., Gagné, J., Popinchalk, M., et al. 2021, ApJ, 923, 48
Filippazzo, J. C., Rice, E. L., Faherty, J., et al. 2015, ApJ, 810, 158
Gagné, J., Faherty, J. K., Cruz, K. L., et al. 2015a, ApJS, 219, 33
Gagné, J., Mamajek, E. E., Malo, L., et al. 2018a, ApJ, 856, 23
Gagné, J., Allers, K. N., Theissen, C. A., et al. 2018b, ApJL, 854, L27
Gaia Collaboration, Vallenari, A., Brown, A. G. A., et al. 2022, arXiv:2208.00211
Gauza, B., Béjar, V. J. S., Pérez-Garrido, A., et al. 2015, ApJ, 804, 96
Gizis, J. E., Faherty, J. K., Liu, M. C., et al. 2012, AJ, 144, 94
Gorlova, N. I., Meyer, M. R., Rieke, G. H., et al. 2003, ApJ, 593, 1074
Helling, Christiane, Woitke, Peter, Rimmer, Paul, et al. 2014, Life, 4, 142
Hiranaka, K., Cruz, K. L., Douglas, S. T., et al. 2016, ApJ, 830, 96
Hsu, C.-C., Burgasser, A. J., Theissen, C. A., et al. 2021, ApJS, 257, 45
Irwin, M. J., Lewis, J., Hodgkin, S., et al. 2004, Proc. SPIE, 5493, 411
Kammerer, J., Lacour, S., Stolker, T., et al. 2021, A&A, 652, A57
Karalidi, T., Apai, D., Schneider, G., et al. 2015, ApJ, 814, 65
Kellogg, K., Metchev, S., Geißler, K., et al. 2015, AJ, 150, 182
Kirkpatrick, J. D., Reid, I. N., Liebert, J., et al. 1999, ApJ, 519, 802
Kirkpatrick, J. D., Reid, I. N., Liebert, J., et al. 2000, AJ, 120, 447
Kirkpatrick, J. D. 2005, ARA&A, 43, 194
Kirkpatrick, J. D., Barman, T. S., Burgasser, A. J., et al. 2006, ApJ, 639, 1120
Kirkpatrick, J. D., Cruz, K. L., Barman, T. S., et al. 2008, ApJ, 689, 1295
Kirkpatrick, J. D., Looper, D. L., Burgasser, A. J., et al. 2010, ApJS, 190, 100
Kirkpatrick, J. D., Gelino, C. R., Faherty, J. K., et al. 2021, ApJS, 253, 7
Khandrika, H., Burgasser, A. J., Melis, C., et al. 2013, AJ, 145, 71
Konopacky, Quinn M., Barman, Travis S., Macintosh, Bruce A., & Marois, Christian 2013, Sci, 339, 1398
Kuchner, M. J., Faherty, J. K., Schneider, A. C., et al. 2017, ApJL, 841, L19
Kuzuhara, M., Currie, T., Takarada, T., et al. 2022, ApJL, 934, L18
Lang, D. 2014, AJ, 147, 108
Lawrence, A., Warren, S. J., Almaini, O., et al. 2007, MNRAS, 379, 1599
Linsky, J. L. 1969, ApJ, 156, 989
Liu, M. C., Dupuy, T. J., & Allers, K. N. 2013a, AN, 334, 85
Liu, M. C., Magnier, E. A., Deacon, N. R., et al. 2013b, ApJL, 777, L20
Liu, M. C., Dupuy, T. J., & Allers, K. N. 2016, ApJ, 833, 96
Livingston, W., & Wallace, L. 1991, NSO Technical Report (Tucson, AZ: National Solar Observatory, National Optical Astronomy Observatory)
Lodieu, N., Zapatero Osorio, M. R., Bejar, V. J. S., & Pena Ramirez, K. 2018, MNRAS, 473, 2020
Looper, D. L., Kirkpatrick, J. D., & Burgasser, A. J. 2007, AJ, 134, 1162
Looper, D. L., Kirkpatrick, J. D., Cutri, R. M., et al. 2008, ApJ, 686, 528
Luhman, K. L., Liebert, J., & Rieke, G. H. 1997, ApJL, 489, L165
Mace, G. N., Kirkpatrick, J. D., Cushing, M. C., et al. 2013, ApJS, 205, 6
Mace, G. N. 2015, in 18th Cambridge Workshop on Cool Stars, Stellar Systems, and the Sun, ed. G. van Belle & H. C. Harris (Flagstaff, AZ: Lowell Observatory), 997
Macintosh, B., Graham, J. R., Barman, T., et al. 2015, Sci, 350, 64
Madhusudhan, N., Burrows, A., & Currie, T. 2011, ApJ, 737, 34
Magnier, E. A., Schlafly, E. F., Finkbeiner, D. P., et al. 2020, ApJS, 251, 6
Mainzer, A., Grav, T., Bauer, J., et al. 2011, ApJ, 743, 156
Mainzer, A., Bauer, J., Cutri, R. M., et al. 2014, ApJ, 792, 30
Manjavacas, E., Bonnefoy, M., Schlieder, J. E., et al. 2014, A&A, 564, A55
Manjavacas, E., Lodieu, N., Bejar, V. J. S., et al. 2020, MNRAS, 491, 5925
Marley, M. S., Saumon, D., Visscher, C., et al. 2021, ApJ, 920, 85
Marocco, F., Day-Jones, A. C., Lucas, P. W., et al. 2014, MNRAS, 439, 372
Marocco, F., Eisenhardt, P. R. M., Fowler, J. W., et al. 2021, ApJS, 253, 8
Marois, Christian, Macintosh, Bruce, Barman, Travis, et al. 2008, Sci, 322, 1348
Martin, E. L., Rebolo, R., & Zapatero-Osorio, M. R. 1996, ApJ, 469, 706
Martinez, R. A., & Kraus, A. L. 2022, AJ, 163, 36
McMahon, R. G., Banerji, M., Gonzalez, E., et al. 2013, Msngr, 154, 35
McGovern, M. R., Kirkpatrick, J. D., McLean, I. S., et al. 2004, ApJ, 600, 1020
Meisner, A. M., Lang, D., & Schlegel, D. J. 2018, RNAAS, 2, 1
Meisner, A. M., Schneider, A. C., Burgasser, A. J., et al. 2021, ApJ, 915, 120
Meisner, A. M., Caselden, D., Schlafly, E. F., et al. 2023, AJ, 165, 36
Meshkat, T., Gao, P., Lee, E. J., et al. 2021, ApJ, 917, 62
Messina, S., Lanzafame, A. C., Feiden, G. A., et al. 2016, A&A, 596, A29
Metchev, S. A., & Hillenbrand, L. A. 2006, ApJ, 651, 1166
Metchev, S. A., Kirkpatrick, J. D., Berriman, G. B., et al. 2008, ApJ, 676, 1281
Metchev, S. A., Heinze, A., Apai, D., et al. 2015, ApJ, 799, 154
Miles, B. E., Skemer, A. J., Barman, T. S., et al. 2018, ApJ, 869, 18
Miles, B. E., Biller, B. A., Patapis, P., et al. 2022, arXiv:2209.00620
Miles-Páez, P. A., Metchev, S., Luhman, K. L., et al. 2017, AJ, 154, 262
Milli, J., Hibon, P., Christiaens, V., et al. 2017, A&A, 597, L2
Miret-Roig, N., Galli, P. A. B., Brandner, W., et al. 2020, A&A, 642, A179
Mohanty, S., Jayawardhana, R., Huélamo, N., et al. 2007, ApJ, 657, 1064
NEOWISE Team 2020, NEOWISE-R Single Exposure (L1b) Source Table, IPAC, doi:10.26131/IRSA144
Nielsen, E. L., De Rosa, R. J., Wang, J., et al. 2016, AJ, 152, 175
Newton, E. R., Charbonneau, D., Irwin, J., et al. 2014, AJ, 147, 20
Oppenheimer, B. R., Baranec, C., Beichman, C., et al. 2013, ApJ, 768, 24
Patience, J., King, R. R., de Rosa, R. J., et al. 2010, A&A, 517, A76
Radigan, J., Jayawardhana, R., Lafrenière, D., et al. 2012, ApJ, 750, 105
Rajan, A., Rameau, J., De Rosa, R. J., et al. 2017, AJ, 154, 10
Reid, I. N., Lewitus, E., Allen, P. R., et al. 2006, AJ, 132, 891
Riedel, A. R., Blunt, S. C., Lambrides, E. L., et al. 2017, AJ, 153, 95
Schapera, N., Caselden, D., Meisner, A. M., et al. 2022, RNAAS, 6, 189
Schneider, A. C., Cushing, M. C., Kirkpatrick, J. D., et al. 2014, AJ, 147, 34
Schneider, A. C., Greco, J., Cushing, M. C., et al. 2016a, ApJ, 817, 112
Schneider, A. C., Windsor, J., Cushing, M. C., et al. 2016b, ApJL, 822, L1
Schneider, A. C., Windsor, J., Cushing, M. C., et al. 2017, AJ, 153, 196
Schneider, A. C., Hardegree-Ullman, K. K., Cushing, M. C., et al. 2018, AJ, 155, 238
Schneider, A. C., Vrba, F. J., Munn, J. A., et al. 2022, AJ, 163, 242
Scholz, R.-D., McCaughrean, M. J., Lodieu, N., et al. 2003, A&A, 398, L29
Shkolnik, E. L., Allers, K. N., Kraus, A. L., et al. 2017, AJ, 154, 69
Skrutskie, M. F., Cutri, R. M., Stiening, R., et al. 2006, AJ, 131, 1163
Softich, E., Schneider, A. C., Patience, J., et al. 2022, ApJL, 926, L12
Steele, I. A., & Jameson, R. F. 1995, MNRAS, 272, 630

Stumpf, M. B., Brandner, W., Bouy, H., et al. 2010, A&A, 516, A37
Suárez, G., & Metchev, S. 2022, MNRAS, 513, 5701
Theissen, C. A., Burgasser, A. J., Martin, E. C., et al. 2022, RNAAS, 6, 151
Thompson, M. A., Kirkpatrick, J. D., Mace, G. N., et al. 2013, PASP, 125, 809
Tremblin, P., Chabrier, G., Baraffe, I., et al. 2017, ApJ, 850, 46
Vacca, W. D., Cushing, M. C., & Rayner, J. T. 2003, PASP, 115, 389
Vos, J. M., Allers, K. N., & Biller, B. A. 2017, ApJ, 842, 78
Vos, J. M., Biller, B. A., Bonavita, M., et al. 2019, MNRAS, 483, 480
Vos, J. M., Biller, B. A., Allers, K. N., et al. 2020, AJ, 160, 38
Vos, J. M., Faherty, J. K., Gagné, J., et al. 2022a, ApJ, 924, 68
Vos, J. M., Burningham, B., Faherty, J. K., et al. 2022b, arXiv:2212.07399
Ward-Duong, K., Patience, J., Follette, K., et al. 2021, AJ, 161, 5
Wilson, J. C., Henderson, C. P., Herter, T. L., et al. 2004, Proc. SPIE, 5492, 1295
WISE Team 2020a, WISE All-Sky Single Exposure (L1b) Source Table, IPAC, doi:10.26131/IRSA139
WISE Team 2020b, WISE 3-Band Cryo Single Exposure (L1b) Source Table, IPAC, doi:10.26131/IRSA127
WISE Team 2020c, NEOWISE 2-Band Post-Cryo Single Exposure (L1b) Source Table, IPAC, doi:10.26131/IRSA124
WISE Team 2020d, WISE All-Sky 4-band Atlas Coadded Images, IPAC, doi:10.26131/IRSA153
Wright, E. L., Eisenhardt, P. R. M., Mainzer, A. K., et al. 2010, AJ, 140, 1868
Yang, H., Apai, D., Marley, M. S., et al. 2016, ApJ, 826, 8
Zhang, Z., Liu, M. C., Hermes, J. J., et al. 2020, ApJ, 891, 171
Zhang, Z., Liu, M. C., Best, W. M. J., et al. 2021, ApJ, 911, 7
Zhou, Y., Bowler, B. P., Morley, C. V., et al. 2020, AJ, 160, 77
Zhou, Y., Bowler, B. P., Apai, D., et al. 2022, AJ, 164, 239
Zuckerman, B., Song, I., Bessell, M. S., et al. 2001, ApJL, 562, L87
Zuckerman, B., Song, I., & Bessell, M. S. 2004, ApJL, 613, L65